

# Lawrence Berkeley National Laboratory

## LBL Publications

### Title

Observation of spin-polarized directive coupling of light at bound states in the continuum

### Permalink

<https://escholarship.org/uc/item/4162m999>

### Journal

Optica, 6(10)

### ISSN

2334-2536

### Authors

Zito, Gianluigi  
Romano, Silvia  
Cabrini, Stefano  
[et al.](#)

### Publication Date

2019-10-20

### DOI

10.1364/optica.6.001305

Peer reviewed



## Observation of spin-polarized directive coupling of light at bound states in the continuum

GIANLUIGI ZITO,<sup>1,4</sup>  SILVIA ROMANO,<sup>2</sup>  STEFANO CABRINI,<sup>3</sup> GIUSEPPE CALAFIORE,<sup>3</sup>  
ANNA CHIARA DE LUCA,<sup>1</sup> ERIKA PENZO,<sup>3</sup> AND VITO MOCELLA<sup>2,5</sup>

<sup>1</sup>National Research Council, Institute of Protein Biochemistry, Via Pietro Castellino, Naples 80131, Italy

<sup>2</sup>National Research Council, Institute of Microelectronics and Microsystems, Via Pietro Castellino, Naples 80131, Italy

<sup>3</sup>National Research Laboratory of Berkeley, Molecular Foundry, Berkeley, California 94720, USA

<sup>4</sup>e-mail: zito.gian@gmail.com

<sup>5</sup>e-mail: vito.mocella@imm.na.cnr.it

Received 20 February 2019; revised 20 June 2019; accepted 16 July 2019 (Doc. ID 360658); published 30 September 2019

Spin-polarized directive coupling of light associated with the photonic quantum spin-Hall effect (QSHE) is a nanoscale phenomenon based on strong spin-orbit interaction that has recently attracted significant attention. Herein, we discuss the experimental manifestation of QSHE intrinsic in the Bloch waves associated with a bound state in the continuum (BIC) of a dielectric photonic crystal metasurface (PhCM). We show numerically that BICs in nanoscale PhCMs have photonic spin angular momentum density transverse to the orbital momentum not only at the interfaces but also inside the confining dielectric medium. Then, we experimentally demonstrate that the fundamental Bloch waves of the BIC mode, macroscopically amplified on resonance, propagate along the symmetry axes of the PhCM obeying spin-momentum locking also at normal incidence, i.e., with no symmetry breaking. This BIC-enhanced spin-directive coupling of light may enable versatile implementations of spin-optical structures, paving the way for novel photonic spin multiplatform devices. © 2019 Optical Society of America under the terms of the OSA Open Access Publishing Agreement

<https://doi.org/10.1364/OPTICA.6.001305>

### 1. INTRODUCTION

The concept of bound state in the continuum (BIC) was introduced by von Neumann and Wigner in quantum mechanics as unusual spatially localized states of electron waves [1]. Later, it was understood that BIC points can occur in the parametric space of all kinds of wave phenomena [2]. In the last years, optical BICs have been demonstrated in engineered photonic crystal metasurfaces (PhCMs) [3–9], either at specific conditions of field symmetry mismatch or topological constraints with respect to out-of-plane propagating waves in free space [10–12]. In particular, the BIC point is associated with a topological singularity in the momentum space [11–15]. Indeed, radiated fields with momentum close to the BIC point have a polarization winding in a vortex structure around the BIC core, as also recently experimentally verified [13,14]. A striking feature is that the electromagnetic field of a BIC is characterized by a diverging lifetime, or an infinite radiative  $Q$ -factor [3,12], from which light-matter interaction could be highly enhanced [16–19]. Reciprocity implies that far-field excitation of an ideal (infinite  $Q$ -factor) BIC mode is not possible. However, real structures can have finite, arbitrarily large  $Q$ -factors close enough to the BIC point, and partial coupling to the input light makes its spectral signature to appear as a special Fano-shaped resonance in quasi-BIC regime, which can be exploited for several applications [17–20]. In addition, of a certain

interest is also the polarization structure of the quasi-BIC radiation [21,22]. As for instance, BIC tuning and structured polarization patterns of radiated light can be produced by suitable in-plane  $C_2$  symmetry breaking [23,24]. Furthermore, unidirectional BICs produced by topological charge bouncing and tuned by broken  $C_{2z}$  symmetry have also been recently demonstrated [25].

Herein, we experimentally find and discuss another phenomenon associated with the intrinsic surface-wave nature of BIC modes in subwavelength PhC thin slabs, the so-called quantum spin-Hall effect (QSHE) of light [26,27]. In solid-state physics, the QSHE is characterized by unique edge states of electrons [28] peculiar of a class of materials termed topological insulators [29]. For time-reversal invariant phases, so-called helical spin-polarized edge states are characterized by spin-momentum locking, i.e., matter waves with opposite spin propagate in opposite directions. Also photonic topological phases that are time-reversal invariant are characterized by two-way spin-polarized directive coupling of light [26,30–32]. In particular, the hallmark of an intrinsic QSHE of light is the transverse spin angular momentum (SAM) density arising in inhomogeneous optical fields [27]. The simplest situation is that of an evanescent wave [26,33,34]. Several experiments have demonstrated the effect of spin-directive coupling in nanoscale dielectric [35–37] and plasmonic [38,39] metasurfaces. As a result of transverse SAM, evanescent waves excited with

opposite spin by virtue of near-field coupling, through nanoparticles [35,39] or quantum emitters [36,37], travel in opposite directions at the interface between two media. This phenomenon of spin-polarized directive coupling [34] enables new quantum-information protocols [36,37,40–47]. However, surface plasmon polaritons in metal are quickly extinguished by absorption and scattering losses. In addition, the efficiency of a nanoparticle-mediated coupling, even in loss-free dielectrics, is limited by the small scattering cross section.

In this work, we discuss the observation of spin-polarized directive coupling of light, in a transparent subwavelength PhCM, achieved as a consequence of the surface wave nature of the BIC mode. We numerically show that the tight nanoscale confinement at the BIC point allows storing high levels of energy inside a highly inhomogeneously structured optical field, thus carrying transverse SAM not only trivially in the evanescent regions but also inside the confining dielectric medium. Experimentally, resonantly enhanced spin-polarized directive coupling of light is demonstrated also in a symmetric excitation condition. The BIC field not only mediates the coupling to the waves characterized by spin-momentum locking but also resonantly amplifies them. This points out exciting opportunities with potential scalability in integrated photonic circuits and chiral quantum technology applications [35,36,41–47]. Indeed, the nearly loss-free dielectric metasurface can be effective for a versatile device implementation. Furthermore, enhancing light–matter interaction at the BIC with concurrent polarization coupling may provide new solutions for spin-optical applications.

## 2. NUMERICAL MODELING AND RATIONALE OF THE PHENOMENON

At normal incidence, a square-lattice PhC thin slab (Fig. 1) has a  $C_{4v}$  point group symmetry. For  $\lambda$  close to the first Bragg

condition  $a \sim \lambda/n_e$ , with  $a$  lattice constant and  $n_e$  effective refractive index, four dominant guided modes exist for each polarization in correspondence to the high symmetry points in the first Brillouin zone [16].

We considered a dielectric geometry consisting of a square lattice of cylindrical air holes etched in a thin film of silicon nitride ( $\text{Si}_3\text{N}_4$ ) [Figs. 1(a)–1(b)] (Supplement 1, Section 1). This material is transparent in both visible and infrared ranges of light and has a real-part refractive index of 2.15 at 532 nm [17]. The unit cell design does not break in-plane inversion symmetry ( $C_2$  symmetry), as visible in Fig. 1(b). Imperfections due to border roughness are randomly oriented and not systematic (tolerance below 1%). These imperfections, together with lattice spacing imperfections, material density fluctuations and absorption loss, finite sample size, and also beam finite collimation eventually allow coupling far-field light with the quasi-BIC mode.

A scheme of the resonator is shown in Fig. 1(c), where the PhCM unit cell is shown with the bottom region made of quartz ( $\text{SiO}_2$ , region 1), i.e., the coverslip experimentally supporting the silicon nitride layer, and top material of air (region 2).

When the excitation radiation tends to zero-transverse wavevector components, i.e.,  $\mathbf{k}_i(\theta_i = 0) = \Gamma = (0, 0, k_z)$ , the dispersion curves  $\omega_n(\mathbf{k}_i)$  climb over the light line, and the confined, guided modes become leaky modes radiating in the far field [10]. However, symmetry incompatibility with free-space modes restores the perfect confinement in the PhCM close to  $\theta_i = 0$ , approaching which the mode  $Q$ -factor diverges, as numerically calculated in Figs. 1(d) and 1(e) for our specific structure. Ideally, the leaky mode becomes a symmetry-protected BIC, of course at specific frequencies depending on the PhCM geometry and composition [3,4]. Numerical modeling was carried out using a rigorous coupled-wave approach (RCWA) [48] and finite element method (COMSOL Multiphysics 5.2a) as detailed in

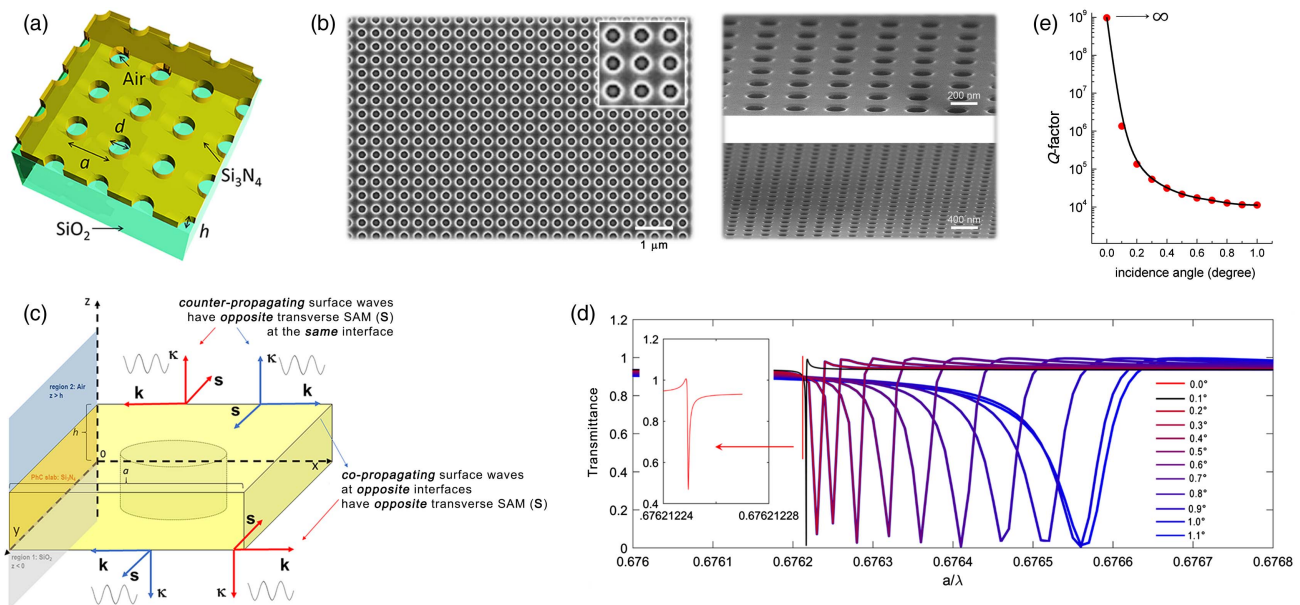


**Fig. 1.** (a) Schematic layout of the PhCM. The experimental sample consists of a square lattice of period  $a$  of cylindrical air holes etched in a silicon nitride ( $\text{Si}_3\text{N}_4$ ) thin film. The silicon nitride film covers all the surface of the supporting quartz substrate ( $\text{SiO}_2$ ), which has thickness 120  $\mu\text{m}$ . The patterned area is 1  $\text{mm}^2$ . (b) Scanning electron microscopy images of the patterned area (inset has sizes of 1  $\mu\text{m}$ ). (c) Spin-momentum locking scheme at the boundaries: the evanescent decay direction  $\boldsymbol{\kappa}$  in the positive and negative  $z$  half spaces locks the relative transverse spin  $\mathbf{s}$  and phase-propagation orientation  $\mathbf{k}$ . (d) Transmittance spectra of the system close to normal incidence showing resonances with a progressively higher  $Q$ -factor. (e) Diverging  $Q$ -factor of the mode approaching normal incidence, corresponding to  $\omega_2 a / 2\pi c = a / \lambda \simeq 0.6762$  in panel (d).

Supplement 1, Section 1. The angular frequency of the lower nontrivial dispersion curve at  $\mathbf{k} = 0$  ( $\Gamma^{(2)}$  point) is  $\omega_a/2\pi c = a/\lambda = 0.67621225$ , as can be seen in the inset of Fig. 1(d). This value corresponds to a BIC point expected to occur at a free-space wavelength  $\lambda_1 = 541.4$  nm for  $a = 365$  nm, in excellent agreement with our experimental findings. The associated mode has a diverging  $Q$ -factor [Fig. 1(e)]. The BIC point occurs at a frequency below the frequencies  $a/\lambda = 1/n = 0.685$  ( $n = 1.46$ ) and  $a/\lambda = 1$  of the modes expected, respectively, in the quartz support and air. The  $\Gamma^{(2)}$  wavevectors, parallel to the  $(x, y)$  plane, have all modulus  $\beta_0 = 2\pi/a$ , i.e., larger than the wavevector modulus both in  $\text{SiO}_2$ , given that  $2\pi/a > 2\pi n/\lambda = k_{\text{SiO}_2}$ , and air, given that  $2\pi/a > 2\pi/\lambda = k_{\text{air}}$ . Since the mode is purely evanescent in regions 1 and 2, at normal incidence, the mode wavevector has a purely imaginary  $z$  component in both regions 1 and 2,  $k_z^{1,2} = \sqrt{k_{\text{air/SiO}_2}^2 - \beta_0^2} \doteq i\kappa_{1,2}$  and cannot couple to the far field. The mode is a Bloch wave exponentially decaying in both  $\pm\hat{z}$ , with a larger decay length in the glass (region 1) since  $\kappa_1 < \kappa_2$ . In the case of purely evanescent fields in regions 1 and 2, the allowed triads of transverse spin  $\mathbf{s}$  and complex wavevector's real part  $\mathbf{k}$  and imaginary part  $\boldsymbol{\kappa}$  according to spin-momentum

locking [34] are depicted in Fig. 1(c) [see Eq. S(2) in Supplement 1, Section 2)].

Figure 2 shows the solutions excited in the case of right-circularly polarized (RCP) and left-circularly polarized (LCP) input plane waves at normal incidence, where convenient finite approximation of the excitation frequency allows far-field source coupling [16]. The degenerate mode excited at normal incidence is a symmetry-protected BIC [4] (diverging lifetime,  $Q > 10^9$ ) with hybrid characteristics of transverse magnetic and electric distributions, with main axial component  $E_z$ . In Figs. 2(a)–2(b), the magnetic field intensity  $|H|^2$  in the PhCM unit cell is superimposed to the arrow maps of the electric field  $\mathbf{E}$  in the  $(x, z)$  plane of the cell border where the field is maximum. Top and bottom panels refer to RCP and LCP incident radiation, respectively. The gray region reproduces the  $\text{Si}_3\text{N}_4$  elementary volume. The  $|H|^2$  profile in the  $z$ -cross section is that of evanescent waves in regions 1 and 2, with larger amplitude at the interface with the  $\text{SiO}_2$ . The field structure  $\mathbf{E}$  appears as a surface wave with strong longitudinal components in the meridional planes. It evolves with cycloidal rotations consistently with the existence of transverse SAM [49] not only trivially in the evanescent regions [30] but also *inside* the PhCM because of the nanoscale confinement.

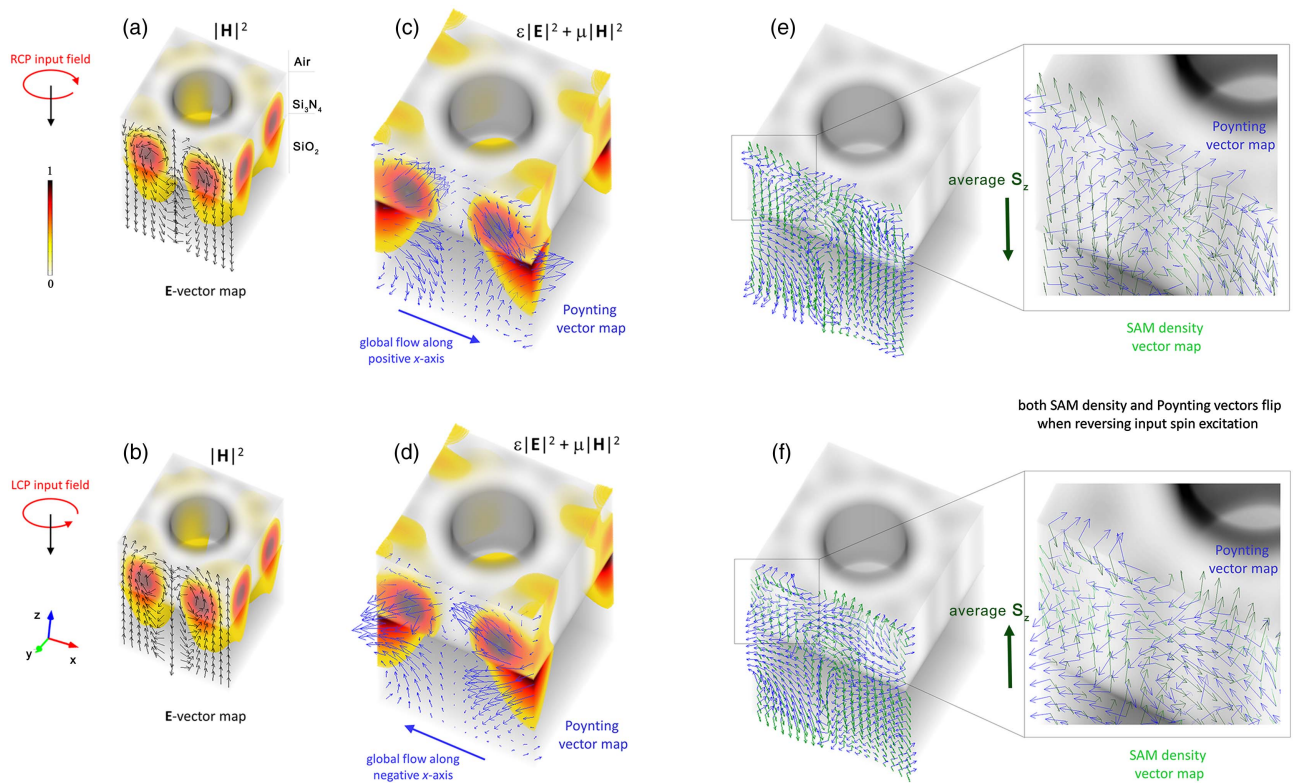


**Fig. 2.** RCWA numerical analysis of the electromagnetic field at the BIC and input SAM dependence. A TM-like BIC mode obtained for  $h = 144$  nm is represented in the unit cell. The top row refers to results obtained for RCP, whereas the second row to LCP excitation. (a), (b). The vector map of the field  $\mathbf{E}$  (uniform magnitude for clarity of representation) shows its character of surface wave and reveals the intriguing behavior of the field excited by opposite circularly polarized input plane waves with opposite orientation of the electric field point by point in (a) and (b). The colormap is associated with magnetic field intensity  $|H|^2$ . The tight confinement produces a significant transverse SAM not only at the interfaces but also inside the nanoscale slab, which locks the propagation direction of the wave along the  $x$  axis depending on the helicity of the input plane wave as can be seen by comparing top and bottom Poynting vector maps in the  $xz$  plane (c), (d) (arrow length is proportional to the vector magnitude). Because of symmetry, an analogous behavior of directional Poynting vector flow occurs also in the  $z$  cross section along  $y$  axis ( $zy$  plane). The colormap is associated with the energy density. In particular, the relative orientation of SAM and Poynting vector can be seen in detail in (e) and (f) (arrow length imposed uniform for better visual inspection for both vectors). It is worth emphasizing that the energy density is much weaker at the interface of the PhC cell with air (top region) as shown in panels (c) and (d); thus, the SAM average  $z$ -axis projection ( $S_z$ ) is that represented by the arrows in (e) and (f). The input spin (scheme on the left) matches the average  $S_z$  of the mode. Since this is transverse to the Poynting vector, as visible in the insets, spin-momentum locking occurs.

The 3D time averaged Poynting vector density  $\mathbf{\Pi} = (1/2)\text{Re}[\mathbf{E} \times \mathbf{H}^*]$  shows reversed vectors orientation from RCP to LCP [Figs. 2(c) and 2(d)], point by point with a vortex structure. Following [33,49] for definition and calculation, we numerically evaluated the SAM density  $\mathbf{S} = \text{Im}[\epsilon_0 \mathbf{E}^* \times \mathbf{E} + \mu_0 \mathbf{H}^* \times \mathbf{H}]/4\omega$  associated with this BIC mode, which resulted in having transverse components with respect to  $\mathbf{\Pi}$ . Indeed, Figs. 2(e)–2(f) show that the SAM always has components orthogonal to the linear momentum density  $\mathbf{\Pi}$  point by point in the unit cell with reversed orientation at the two interfaces, respectively, with SiO<sub>2</sub> (region 1) and with air (region 2), consistent with the spin-momentum locking conditions expected for top and bottom evanescent waves having opposite imaginary wavevectors in the two regions. It is worth mentioning that while this locking mechanism occurs at the boundaries of any optically confining system [34], in the particular case of our nanoscale PhCM at the BIC, the boundaries are so close, with a distance inferior to the same optical wavelength, that the transverse SAM is large also inside the medium where it is resonantly enhanced. Back to Fig. 2, given that the  $(x, y)$  components of the field are comparable in amplitude to the  $z$  component, we can see that the spin density has strong components along  $z$ , which allows spin matching with the  $z$ -directed spin of the input excitation at normal incidence [Figs. 2(e)–2(f)]. Since the spin-momentum locking is a boundary condition that selects the waveguiding direction, of the four possible wave solutions at the boundaries, only two can be excited by a given input spin and correspond to counter-propagating surface waves at the two dielectric interfaces [Fig. 1(c)]. The boundary spin structure is consistent with the spin structure of the mode inside the confining dielectric, which is on the other hand determined by the spin matching with input light. Importantly, we can easily see from the asymmetry of the mode profile along the  $z$  axis in Figs. 2(c)–2(d) that these two waves have different amplitudes at the interfaces. Along a given direction, say  $x$  axis in Fig. 2, in one way, there will be more light than the way back for a given input circular polarization, with reversed behavior for the opposite input helicity. Therefore, we can say that the input spin matching selects two surface waves that, if out-coupled again in free space, will be characterized by a different field intensity, depending on the input spin causing a breaking of the planar mirror symmetry of the system even at normal incidence, with a macroscopic spin-polarized directive coupling.

Figures S2 and S3 in Supplement 1 show that transverse SAM exists also in the case of a quasi-BIC and in case of a non-symmetry-protected BIC [5], existing for different values of  $h$ .

### 3. BIC SPIN-ORBIT ASYMMETRY PHENOMENOLOGY AND CHARACTERIZATION

Several 1 – mm<sup>2</sup> PhCMs of Si<sub>3</sub>N<sub>4</sub> were fabricated with various thicknesses (Supplement 1, Section 3), as also shown in Fig. 1(b). Herein, we will focus our attention on the case of  $h = 144$  nm, where the expected BIC mode in Fig. 2 emerges at 541.4 nm. A schematic layout of the optical characterization of the PhCM is shown in Fig. 3(a). The PhCM is placed at the center of the supporting glass coverslip and illuminated with a collimated super-continuum laser source to measure the transmission spectrum and to identify the characteristic resonances of interest (Supplement 1, Section 3). The PhCM transmission spectrum collected at normal incidence  $\theta_i = 0^\circ$  is shown in Fig. 3(b). Two spectral dips are visible at  $\lambda_1 = 541.4$  nm and  $\lambda_2 = 550.0$  nm, corresponding,

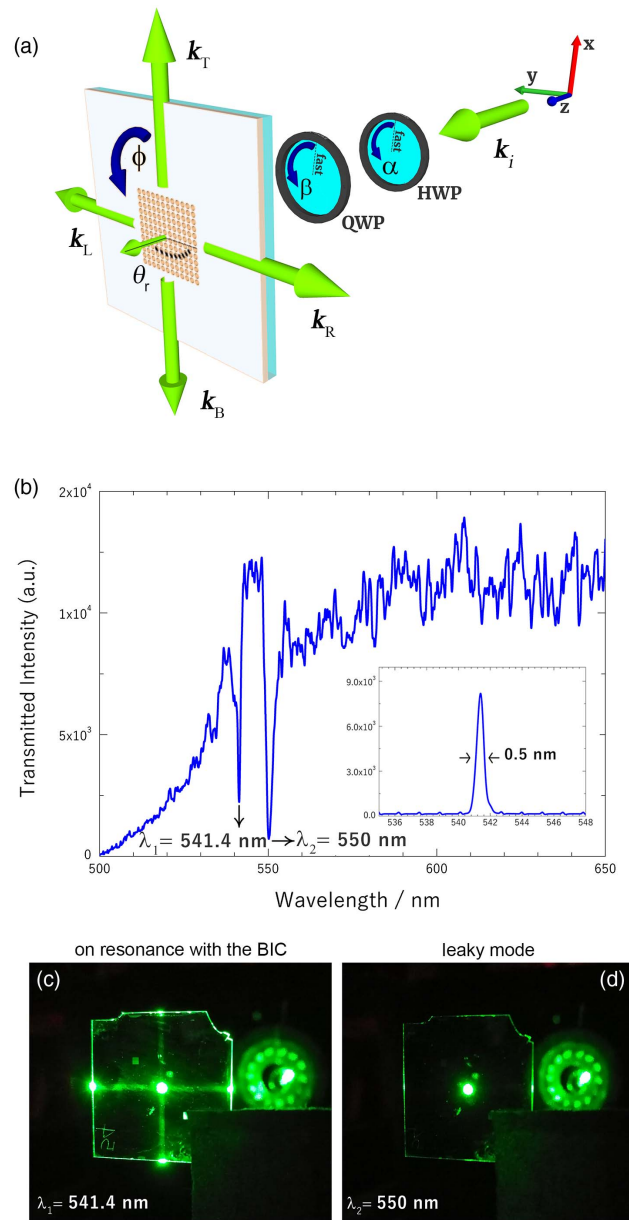


**Fig. 3.** Phenomenology of the redirection effect at the BIC. (a) Schematic layout of the experimental setup. The input beam polarization  $\mathbf{E}_i$  (initially  $\parallel \hat{x}$ ) is controlled by means of a half-wave plate (HWP) and a quarter-wave plate (QWP). At the BIC frequency, light is redirected at  $\theta_r = \pi/2$  along the PhC axes of symmetry. (b) Normal incidence transmission spectrum of a PhCM designed to support a BIC in the visible range. Two modes are visible:  $\lambda_1$  corresponds to a near-BIC regime, whereas  $\lambda_2$  to a conventional leaky mode. (c) At the BIC wavelength  $\lambda_1$ , the normally incident light is experimentally redirected along the PhC symmetry axes (LCP input in figure). The inset of the spectrum in (b) shows the far-field spectral profile of the redirected beam of wave-vector  $\mathbf{k}_R$  collected from the side. (d) At  $\lambda_2$ , there is no detectable redirection effect at any input polarization (LCP input in figure).

respectively, to the BIC point and to a lower  $Q$ -factor mode (leaky mode). It is worth noticing that the total  $Q$ -factor of the BIC is limited by finite sample size ( $Q_H$ ), effective collimation, and scattering losses due to the sample imperfections ( $Q_A$ ) (Supplement 1, Section 3) [50]. As such, we measured a total  $Q \sim 10^3$  corresponding to a linewidth  $\simeq 0.5$  nm [Fig. 3(b)], due mainly to finite

lateral confinement and surface roughness, in agreement with previous papers [3,50].

We used an acousto-optical tunable filter to tune the incident wavelength to  $\lambda_1$  [Fig. 3(c)] or  $\lambda_2$  [Fig. 3(d)]—with linewidth  $\sim 4$  nm. At  $\lambda_1$ , the peak incident intensity  $I_{in}$  of the transmitted beam through the sample decreased by about 80%, showing a clear dip with 0.5-nm width (Fig. S4). When the light source is resonant with this BIC, the light trapped inside the metasurface positioned at the center of the supporting glass [the green laser spot in Fig. 3(c)] generates four coherent collimated beams propagating along the four-fold symmetry directions of the PhCM. The representative image in Fig. 3(c) is obtained with LCP excitation. A significant fraction of the input intensity  $I_{in}$  is conveyed to these beams, which we will term *side waves*, with typically  $0.1I_{in}$  per wave detected in the far field on the sides of the sample. We indicate the observed side waves by their wavevectors,  $\mathbf{k}_R = -\beta_0\hat{y}(R)$ ,  $\mathbf{k}_L = +\beta_0\hat{y}(L)$ ,  $\mathbf{k}_T = +\beta_0\hat{x}(T)$ ,  $\mathbf{k}_B = -\beta_0\hat{x}(B)$ , as displayed in the scheme reported in Fig. 3(a).

Conversely, at  $\lambda_2$  (leaky mode), no light was visible around the PhCM [center spot, Fig. 3(d)]. The intensity of the light possibly leaking on the sides of the sample was on the order of the detector noise level, i.e., at least four orders of magnitude less intense than the side waves observed at the BIC.

We interpreted these side waves generated at the BIC wavelength as the first four fundamental Bloch's waves  $\Gamma^{(2)}$  composing the BIC mode, thus intrinsically amplified by the resonant mechanism (see additional text in Supplement 1, Section 2).

Given the geometry of the lattice and the input wavelength, if we examine the PhCM as a basic two-dimensional diffraction grating, the Bragg law implies that at normal incidence, the first orders of diffraction have complex wavevectors, since these first-order waves are evanescent and have phase wavevectors parallel to the structure plane. When the input wavelength matches the singular point defined by the BIC, the resonant mechanism feeds such diffracted waves, which actually compose the mode, and makes them easily detectable even in the far field. Trivially, the rotation of the PhCM about the  $z$  axis of an angle  $\phi$  produces an equal rotation of the side waves, which are therefore uniquely associated with the geometry of the system.

Now, these side waves, which are collected back in free space and characterized [Fig. 4(a)], have linear momenta in the  $(x, y)$  plane of the PhCM, and the optical field generating them is characterized by a transverse SAM (Fig. 2). As a consequence, the symmetry breaking due to spin-orbit, as discussed in the previous section, is expected to affect the intensity of the radiation (out-coupled along a specific wavevector) as a function of input polarization. Indeed, the surface wave at the air/Si<sub>3</sub>N<sub>4</sub> boundary is more tightly confined and weaker than the wave at the Si<sub>3</sub>N<sub>4</sub>/SiO<sub>2</sub> interface, as can be seen in Figs. 2(c)–2(d). This last can propagate at the interface Si<sub>3</sub>N<sub>4</sub>/SiO<sub>2</sub>, since the Si<sub>3</sub>N<sub>4</sub> covers all quartz areas, and partly leaks to the quartz substrate where it is guided and then measured in the far field. A scheme is depicted in Fig. S5 (Supplement 1).

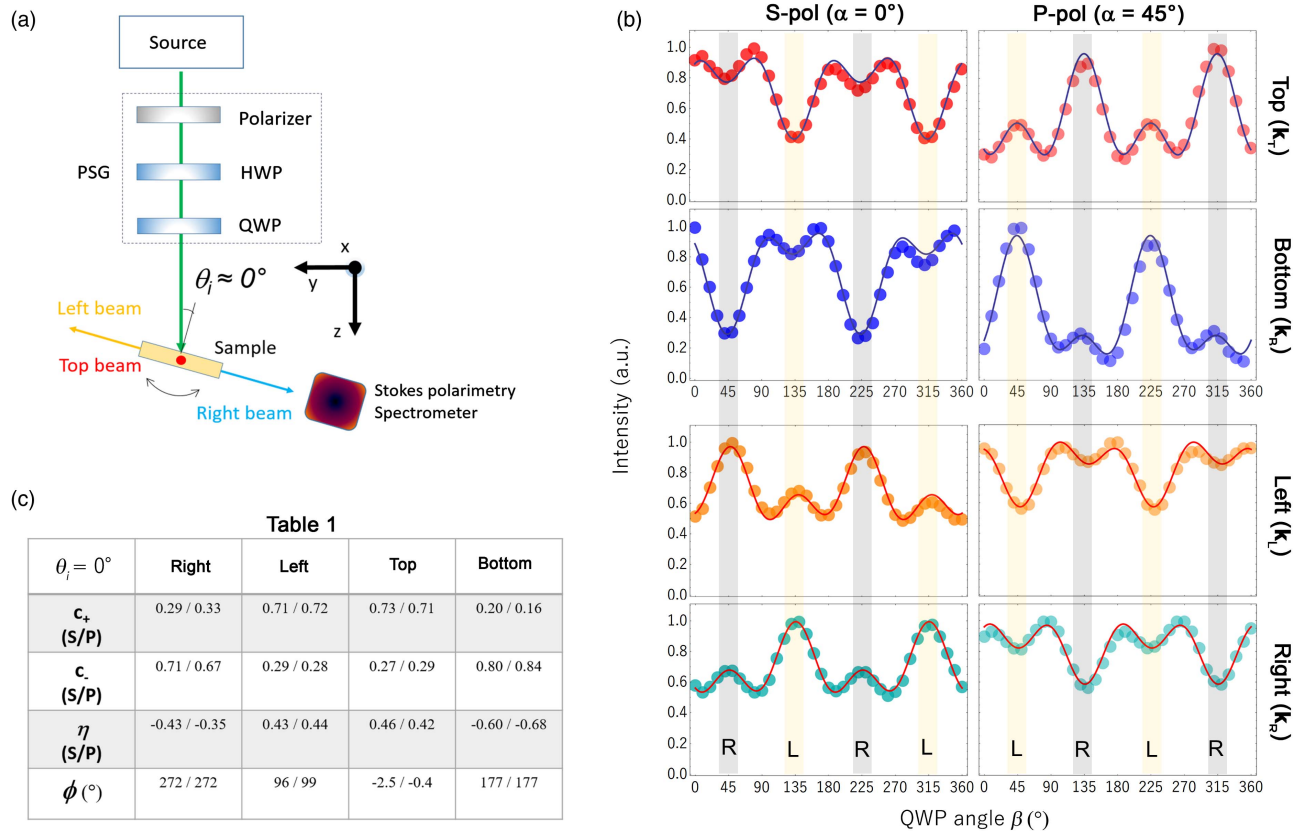


**Fig. 4.** Asymmetric spin-orbit behavior at the BIC ( $\theta_i = 0^\circ$ ). (a) General layout of the far-field characterization with the PhCM axes parallel to the laboratory reference system. (b) Intensity of the side waves outcoupled from the PhCM measured as function of the QWP angle  $\beta$  for input  $s$  and  $p$  polarization for  $\theta_i = 0^\circ$ . The experimental points show a macroscopic chiral behavior. The solid lines are the curves obtained with the model fit, which show an excellent agreement with the data. (c) The chiral parameters resulting from the fit are indicated in Table 1: S/P indicates that the values are, respectively, referred to  $s$ -pol or  $p$ -pol of (b).

A similar spin-polarized directive coupling in a rotationally symmetric nanoscale structure has been experimentally observed by Petersen *et al.* [35] in the case of a two-fold symmetric optical nanofiber illuminated by circularly polarized light at normal incidence, indeed despite the rotational invariance of the configuration. In that case, there was an evanescent coupling provided by the light scattering of a gold nanoparticle. In our case, the scattering element is the cylindrical hole (coupled with the other ones in a lattice resonance). The resonant field has transverse SAM inside the confining region because of nanoscale localization. Thus, it is the very intrinsic nature of the eigenmode to determine the Poynting vector flow that obeys spin-momentum locking (see additional text in Supplement 1, Section 2).

Tunable waveplate retarders were used to set the input polarization  $\mathbf{E}_i$  with a polarization-state generator (PSG) consisting of a polarizer (axis //  $\hat{\mathbf{x}}$ ), a half-wave plate (HWP), and a quarter-wave plate (QWP). The layout of the experiment is shown in Fig. 4(a). The Jones optical transformation of the input beam is detailed in Supplement 1, Section 4. The intensity  $I_j(\alpha, \beta)$  of the side waves ( $j \in \{R, L, T, B\}$ ) was measured as a function of the angle  $\beta$  (QWP) for fixed values of  $\alpha$  (HWP) [see also Fig. 3(a)]. The measurements shown in Fig. 4(b) were carried out at  $\theta_i = 0$ . In particular, we fixed the HWP angle  $\alpha$  to two values,  $\alpha^S = 0^\circ$  (S-polarized input on the QWP) and  $\alpha^P = 45^\circ$  (P-polarized input on the QWP), whereas  $\beta$  was varied in the range  $(0, 360^\circ)$ . This means that the handedness of the circular polarization generated by the QWP is reversed by switching  $\alpha^S$  to  $\alpha^P$ , which we used to check any possible spurious dependence due to optical misalignment.

Comparing the curves for the bottom side wave ( $\mathbf{k}_B$ ) in Fig. 4(b) that were obtained for  $\alpha^S$  (left panel) with that for  $\alpha^P$  (right panel), we can observe that when the input state is LCP, the intensity measured in the bottom side wave is always maximum. In other words, LCP light is coupled preferentially to the propagation direction  $\mathbf{k}_B$ , in agreement with the simulation for LCP input excitation in Figs. 2(b)–2(d) ( $\mathbf{k}_B = -\beta_0 \hat{\mathbf{x}}$ ). On the other hand, input RCP light is instead preferentially coupled to the propagation direction  $\mathbf{k}_T$  along positive  $x$  axis. Actually, this behavior can be verified also on the side waves  $R$  and  $L$ . Indeed, in Fig. 4(b), we can observe a clear dependence in  $I(\beta)$  on the handedness of the input polarization for all the side waves, with anti-correlated behaviors between homologous opposite beams, i.e., between waves  $R$  and  $L$ , and waves  $T$  and  $B$ .

When the exciting incident SAM (parallel to  $\hat{\mathbf{z}}$ ) couples to the transverse spin of the BIC mode, it locks to the photon flow mediated by the BIC transverse SAM components ( $z$ -component on average), which induces opposite propagation directions in the  $(x, y)$  plane of the fundamental Bloch's waves composing the mode, as shown in the simulations in Fig. 2. The resonant mechanism of the BIC is then responsible for the macroscopic nature of this spin-polarized directive coupling.

It is worth stressing that our PhC unit cell, having a cylindrical hole, does not break in-plane  $C_2$  inversion symmetry. Such a symmetry breaking would be responsible for splitting the BIC topological charge (destroying the BIC singularity) into a couple of circularly polarized states of half-integer charge, which can radiate in the far field along directions at opposite angles very close to the normal direction [24]. In our case, instead, the chiral behavior is observed in the light radiated from the Bloch's wave components of the BIC in the plane of the PhC, i.e., at  $90^\circ$  with respect to the

normal incidence, a phenomenon that is related to the intrinsic nature of a surface wave of the eigenmode and its SAM orientation, transverse to the momentum.

#### 4. PHENOMENOLOGICAL MODEL

Also in the case of linear input polarization (QWP angle  $\beta = 0^\circ$ ), symmetry breaking is visible in the experimental data in Fig. 4(b) between  $\hat{\mathbf{x}}$  ( $T, B$ ) and  $\hat{\mathbf{y}}$  ( $L, R$ ) waves. When the input field is not spin polarized, i.e., the input is  $s$  or  $p$  polarized, the response of the system can be seen in terms of the coupling to a surface wave, which in the first place has an axial field component  $E_z$ . Supposing an  $s$ -polarized input field  $(E_x, 0, 0)$  [Fig. 3(a)], then the surface wave  $(E_x, H_y, E_z)$  propagating along the  $x$  axis is favored, having a longitudinal component  $E_x$  that is conserved by tangential component continuity. For  $p$ -polarized input  $(0, E_y, 0)$ , the waves directed along the  $y$  axis are similarly favored, again for matching of the field structure of a surface wave along that direction.

We built a phenomenological model to fit the intensity of the side waves, out-coupled in the far field, for all possible input states of polarization. We modeled the scattering of photons from the incidence direction  $\hat{\mathbf{z}}$  to the  $(x, y)$  plane, considering that redirection is accompanied by nonparaxial spin-to-angular momentum conversion [27,49,51–54], as fully detailed in Supplement 1, Section 4.

The polarization  $\mathbf{E}_i$  incident on the sample depends on the wave plate retarder angles  $\alpha$  and  $\beta$ , while the transformation  $\hat{U}$  due to redirection introduces dependence on the orientation angles  $\theta_r = \pi/2$  and  $\phi$  in the  $(x, y)$  plane [Fig. 3(a)]. In particular, we considered  $\phi$  to assume only four discrete values determined by the four-fold symmetry of the PhCM lattice as verified experimentally [Fig. 3(c)]. Compacting the variables of interest in the vector form  $\mathbf{v}_j \equiv (\alpha, \beta, \phi_j)$ , with  $j \in \{R, L, T, B\}$  (Supplement 1, Section 4), in the circular polarization basis with output field components  $\{E_w^+, E_w^-, E_w^z\}$ , we can write

$$I(\mathbf{v}_j) = c_+ |E_w^+(\mathbf{v}_j)|^2 + c_- |E_w^-(\mathbf{v}_j)|^2 + c_z |E_w^z(\mathbf{v}_j)|^2, \quad (1)$$

with  $j \in \{R, L, T, B\}$ ,  $\theta_r = \pi/2$  and  $\phi_T = 0^\circ$ ,  $\phi_L = 90^\circ$ ,  $\phi_B = 180^\circ$ , and  $\phi_R = 270^\circ$ . In the above expression, the output intensity of the field redirected along a PhCM symmetry axis is written in terms of its circular and longitudinal polarization components along the direction of propagation. Since the side waves possess a transverse SAM, which the direction of propagation is locked to, in the above expression, we balance the components with the coefficients  $c_\pm$  admitting values in the range  $(0, 1)$  to account for a possible *spin-polarized* coupling of input light to the mode (Fig. 2). In the case of  $\{c_+ = 1, c_- = 0, c_z = 0\}$ , for instance, light would be right-handed circularly polarized. Similarly,  $\{c_+ = 0, c_- = 1, c_z = 0\}$  would correspond to an LCP state. These coefficients were used as parameters when fitting the experimental data in Figs. 4 and 5, quantifying the parameter of *chiral directivity* defined as  $\eta = \frac{c_+ - c_-}{c_+ + c_-}$  [35]. In absence of spin-polarized coupling along a given observation direction  $\phi_j$ ,  $j \in \{R, L, T, B\}$ , since RCP and LCP states would have no preferential coupling, then  $c_+ = c_-$  and  $\eta = 0$ ; thus, for each  $\phi_j$ , the intensity becomes  $I(\beta) = I(\beta + m\pi/2)$ , with  $m$  integer, i.e., periodic of period  $\pi/2$ . Instead, experimentally, the curves  $I(\beta)$  show a periodic modulation of period  $\pi$ , indeed characterized by the presence of secondary maxima or minima [Fig. 4(b)]. When we include spin-polarized coupling,  $c_+ \neq c_-$ , the side wave intensity does depend on the handedness of the polarization,

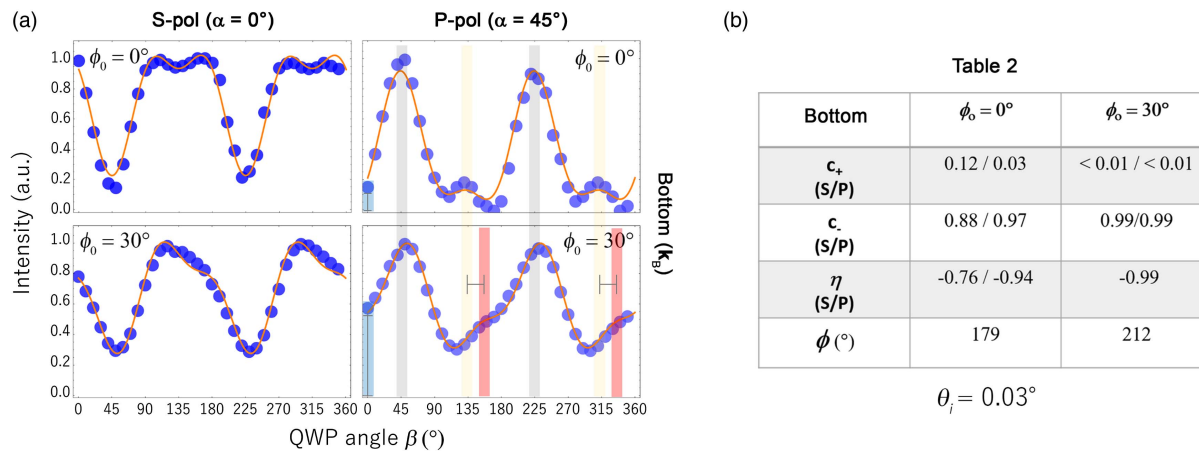


**Fig. 5.** Chiral behavior with broken symmetry excitation ( $\theta_i = 0.03^\circ$ ) and geometric phase effect. (a) Intensity of the redirected bottom side wave measured as function of the QWP angle  $\beta$  for input  $s$  and  $p$  polarization. Measurements were carried out at  $\theta_i = 0.03^\circ$ . Top panels report the case  $\phi_0 = 0^\circ$ , whereas bottom panels the case  $\phi_0 = 30^\circ$ . (b) Table 2 reports the fit parameters with a chiral directivity  $\eta$  close to 1. S/P indicates that the values are respectively referred to  $s$ -pol or  $p$ -pol of (a).

which explains the period  $\pi$  and fits the experimental data as a function of the direction, as shown in Fig. 4(b). In Fig. 4(c) (Table 1), we report the fit parameters and the estimated chiral directivity  $\eta$ . The fit coefficient  $c_z$  is below 1%, consistent with a far-field detection scheme for which no longitudinal components may exist along the propagation, and thus is not reported. The value  $|\eta|$  varies from 32% to 68% at  $\theta_i = 0^\circ$ .

In addition, in Fig. 4(b), once fixed, the side wave, by comparing left and right panels, we can see that by exchanging  $\alpha$  from  $0^\circ$  to  $45^\circ$ , an intensity reversal occurs as a function of  $\beta$ . This is due to the geometric phase shift introduced by the HWP, which is well predicted by the model and further verified in the next data.

In Fig. 5, we analyze the case of a slight deviation from normal incidence, measuring the intensity of the side waves for  $\theta_i = 0.03^\circ$ . In this case,  $|\eta|$  reaches the largest value of 94% [Table 2 in Fig. 5(b)]. We ascribe this increased spin-directive coupling to the breaking of the system symmetry due to a non-symmetric excitation condition, which favors the observed chiral coupling. Indeed, the BIC transverse SAM has components also in the PhCM plane (Fig. 2), which may thus influence the overall efficiency of light coupling. Further research is necessary to provide a general comprehension of the phenomenon.

As previously discussed, the side waves follow the axes of the PhCM. The second row in Fig. 5(a) shows the effect of rotating the PhCM about the  $z$ -axis of an angle  $\phi_0 = 30^\circ$ . The rotation with respect to the input polarizer, defining the reference, may be seen as the simple transformation of the geometric phase  $\phi'_j = \phi_j + \phi_0$  for each redirected side wave. As visible in the bottom panel of Fig. 5(a) ( $\phi_0 = 30^\circ$ ), the intensity curves appear shifted in  $\beta$  because of the new  $\phi'_j$  and are characterized by a different overall shape with respect to the case  $\phi_0 = 0^\circ$  (top panel). This can be appreciated, for instance, by the different values measured at  $\beta = 0^\circ$ . The agreement with the model fit is also in this case very good, with an estimated directivity  $|\eta| = 99.9\%$  (Table 2).

## 5. CONCLUSION

Concluding, the optical field at the BIC point of a nanoscale PhCM is characterized by strong transverse SAM components

that are induced by the tight confinement of the electromagnetic field and that can be used to devise macroscopic spin-orbit interactions. Experimentally, we have shown that the BIC resonantly feeds the fundamental Bloch's surface waves of the mode, providing macroscopic spin-momentum-locked propagation along the symmetry axes of the PhCM. Since a resonator in the BIC regime is characterized by strong near-field amplification, engineering such high  $Q$ -factor resonators may lead to metasurface multiplex applications, also favored by the large-scale collective character of the BIC that makes the resonator intrinsically robust against external perturbations. Concurrently, other effects may be enhanced, such as unidirectional low-threshold lasing and strong-coupling regime phenomena, providing novel quantum chiral photonic applications.

**Funding.** Ministero dell'Istruzione, dell'Università e della Ricerca (PRIN 2017 0002501).

**Acknowledgment.** The authors thank Dr. Edoardo De Tommasi for fruitful discussions. G. Z. acknowledges partial support from MIUR grant no. PRIN 2017 0002501.

See Supplement 1 for supporting content.

## REFERENCES

1. J. von Neumann and E. P. Wigner, "Über merkwürdige diskrete Eigenwerte. Über das Verhalten von Eigenwerten bei adiabatischen Prozessen," *Phys. Z.* **30**, 465–467 (1929).
2. H. Friedrich and D. Wintgen, "Interfering resonances and bound states in the continuum," *Phys. Rev. A* **32**, 3231 (1985).
3. C. W. Hsu, B. Zhen, J. Lee, S.-L. Chua, S. G. Johnson, J. D. Joannopoulos, and M. Soljačić, "Observation of trapped light within the radiation continuum," *Nature* **499**, 188–191 (2013).
4. S. Fan and J. Joannopoulos, "Analysis of guided resonances in photonic crystal slabs," *Phys. Rev. B* **65**, 235112 (2002).
5. A. Kodigala, T. Lepetit, Q. Gu, B. Bahari, Y. Fainman, and B. Kanté, "Lasing action from photonic bound states in continuum," *Nature* **541**, 196–199 (2017).
6. J. Gomis-Bresco, D. Artigas, and L. Torner, "Anisotropy-induced photonic bound states in the continuum," *Nat. Photonics* **11**, 232–236 (2017).
7. C. W. Hsu, B. Zhen, A. D. Stone, J. D. Joannopoulos, and M. Soljačić, "Bound states in the continuum," *Nat. Rev. Mater.* **1**, 16048 (2016).

8. K. Koshelev, A. Bogdanov, and Y. Kivshar, "Meta-optics and bound states in the continuum," *Sci. Bull.* **64**, 836–842 (2018).
9. Z. Sadrieva, K. Frizyuk, M. Petrov, Y. Kivshar, and A. Bogdanov, "Multipolar origin of bound states in the continuum," arXiv:1903.00309 (2019).
10. K. Sakoda, *Optical Properties of Photonic Crystals* (Springer Science & Business Media, 2004), Vol. 80.
11. B. Zhen, C. W. Hsu, L. Lu, A. D. Stone, and M. Soljačić, "Topological nature of optical bound states in the continuum," *Phys. Rev. Lett.* **113**, 257401 (2014).
12. L. Lu, J. D. Joannopoulos, and M. Soljačić, "Topological photonics," *Nat. Photonics* **8**, 821–829 (2014).
13. Y. Zhang, A. Chen, W. Liu, C. W. Hsu, B. Wang, F. Guan, X. Liu, L. Shi, L. Lu, and J. Zi, "Observation of polarization vortices in momentum space," *Phys. Rev. Lett.* **120**, 186103 (2018).
14. H. M. Doeleman, F. Monticone, W. den Hollander, A. Alù, and A. F. Koenderink, "Experimental observation of a polarization vortex at an optical bound state in the continuum," *Nat. Photonics* **12**, 397–401 (2018).
15. W. Chen, Y. Chen, and W. Liu, "Singularities and poincaré indices of electromagnetic multipoles," *Phys. Rev. Lett.* **122**, 153907 (2019).
16. V. Mocella and S. Romano, "Giant field enhancement in photonic resonant lattices," *Phys. Rev. B* **92**, 155117 (2015).
17. S. Romano, G. Zito, S. Managò, G. Calafiore, E. Penzo, S. Cabrini, A. C. De Luca, and V. Mocella, "Surface-enhanced Raman and fluorescence spectroscopy with an all-dielectric metasurface," *J. Phys. Chem. C* **122**, 19738–19745 (2018).
18. S. Romano, G. Zito, S. Torino, G. Calafiore, E. Penzo, G. Coppola, S. Cabrini, I. Rendina, and V. Mocella, "Label-free sensing of ultralow-weight molecules with all-dielectric metasurfaces supporting bound states in the continuum," *Photon. Res.* **6**, 726–733 (2018).
19. S. Romano, A. Lamberti, M. Masullo, E. Penzo, S. Cabrini, I. Rendina, and V. Mocella, "Optical biosensors based on photonic crystals supporting bound states in the continuum," *Materials* **11**, 526 (2018).
20. S. Romano, G. Zito, S. N. Lara Yépez, S. Cabrini, E. Penzo, G. Coppola, I. Rendina, and V. Mocella, "Tuning the exponential sensitivity of a bound-state-in-continuum optical sensor," *Opt. Express* **27**, 18776–18786 (2019).
21. C. W. Hsu, B. Zhen, M. Soljačić, and A. D. Stone, "Polarization state of radiation from a photonic crystal slab," arXiv:1708.02197 (2017).
22. W. Ye, Y. Gao, and J. Liu, "Polarization diversity close to the optical bound states in the continuum," arXiv:1904.09597 (2019).
23. F. Yesilkoy, E. R. Arvelo, Y. Jahani, M. Liu, A. Tittl, V. Cevher, Y. Kivshar, and H. Altug, "Ultrasensitive hyperspectral imaging and biodetection enabled by dielectric metasurfaces," *Nat. Photonics* **13**, 390–396 (2019).
24. W. Liu, B. Wang, Y. Zhang, J. Wang, M. Zhao, F. Guan, X. Liu, L. Shi, and J. Zi, "Circularly polarized states spawning from bound states in the continuum," arXiv:1904.01733 (2019).
25. X. Yin, J. Jin, M. Soljačić, C. Peng, and B. Zhen, "Observation of unidirectional bound states in the continuum enabled by topological defects," arXiv:1904.11464 (2019).
26. K. Y. Bliokh, D. Smirnova, and F. Nori, "Quantum spin Hall effect of light," *Science* **348**, 1448–1451 (2015).
27. K. Y. Bliokh, F. Rodríguez-Fortuño, F. Nori, and A. V. Zayats, "Spin-orbit interactions of light," *Nat. Photonics* **9**, 796–808 (2015).
28. C. L. Kane and E. J. Mele, " $z_2$  topological order and the quantum spin Hall effect," *Phys. Rev. Lett.* **95**, 146802 (2005).
29. X.-L. Qi and S.-C. Zhang, "Topological insulators and superconductors," *Rev. Mod. Phys.* **83**, 1057 (2011).
30. K. Y. Bliokh, A. Y. Bekshaev, and F. Nori, "Extraordinary momentum and spin in evanescent waves," *Nat. Commun.* **5**, 3300 (2014).
31. P. Lodahl, S. Mahmoodian, S. Stobbe, P. Schneeweiss, J. Volz, A. Rauschenbeutel, H. Pichler, and P. Zoller, "Chiral quantum optics," *Nature* **541**, 473–480 (2017).
32. A. B. Khanikaev and G. Shvets, "Two-dimensional topological photonics," *Nat. Photonics* **11**, 763 (2017).
33. A. Aiello, P. Banzer, M. Neugebauer, and G. Leuchs, "From transverse angular momentum to photonic wheels," *Nat. Photonics* **9**, 789–795 (2015).
34. T. Van Mechelen and Z. Jacob, "Universal spin-momentum locking of evanescent waves," *Optica* **3**, 118–126 (2016).
35. J. Petersen, J. Volz, and A. Rauschenbeutel, "Chiral nanophotonic waveguide interface based on spin-orbit interaction of light," *Science* **346**, 67–71 (2014).
36. I. Söllner, S. Mahmoodian, S. L. Hansen, L. Midolo, A. Javadi, G. Kiršanskė, T. Pregolato, H. El-Ella, E. H. Lee, J. D. Song, S. Stobbe, and P. Lodahl, "Deterministic photon-emitter coupling in chiral photonic circuits," *Nat. Nanotechnol.* **10**, 775–778 (2015).
37. C. Junge, D. O'shea, J. Volz, and A. Rauschenbeutel, "Strong coupling between single atoms and nontransversal photons," *Phys. Rev. Lett.* **110**, 213604 (2013).
38. L. Huang, X. Chen, B. Bai, Q. Tan, G. Jin, T. Zentgraf, and S. Zhang, "Helicity dependent directional surface plasmon polariton excitation using a metasurface with interfacial phase discontinuity," *Light Sci. Appl.* **2**, e70 (2013).
39. D. O'Connor, P. Ginzburg, F. Rodríguez-Fortuño, G. Wurtz, and A. Zayats, "Spin-orbit coupling in surface plasmon scattering by nanostructures," *Nat. Commun.* **5**, 5327 (2014).
40. R. Mitsch, C. Sayrin, B. Albrecht, P. Schneeweiss, and A. Rauschenbeutel, "Quantum state-controlled directional spontaneous emission of photons into a nanophotonic waveguide," *Nat. Commun.* **5**, 5713 (2014).
41. Y. Liu, Y. Ke, H. Luo, and S. Wen, "Photonic spin Hall effect in metasurfaces: a brief review," *Nanophotonics* **6**, 51–70 (2017).
42. E. Maguid, I. Yulevich, D. Veksler, V. Kleiner, M. L. Brongersma, and E. Hasman, "Photonic spin-controlled multifunctional shared-aperture antenna array," *Science* **352**, 1202–1206 (2016).
43. A. B. Khanikaev, S. H. Mousavi, W.-K. Tse, M. Kargarian, A. H. MacDonald, and G. Shvets, "Photonic topological insulators," *Nat. Mater.* **12**, 233–239 (2013).
44. X. Yin, Z. Ye, J. Rho, Y. Wang, and X. Zhang, "Photonic spin Hall effect at metasurfaces," *Science* **339**, 1405–1407 (2013).
45. N. Shitrit, I. Yulevich, E. Maguid, D. Ozeri, D. Veksler, V. Kleiner, and E. Hasman, "Spin-optical metamaterial route to spin-controlled photonics," *Science* **340**, 724–726 (2013).
46. D. Lin, P. Fan, E. Hasman, and M. L. Brongersma, "Dielectric gradient metasurface optical elements," *Science* **345**, 298–302 (2014).
47. N. Yu, P. Genevet, M. A. Kats, F. Aieta, J.-P. Tetienne, F. Capasso, and Z. Gaburro, "Light propagation with phase discontinuities: generalized laws of reflection and refraction," *Science* **334**, 333–337 (2011).
48. V. Liu and S. Fan, "S<sup>2</sup>: a free electromagnetic solver for layered periodic structures," *Comp. Phys. Commun.* **183**, 2233–2244 (2012).
49. K. Y. Bliokh and F. Nori, "Transverse and longitudinal angular momenta of light," *Phys. Rep.* **592**, 1–38 (2015).
50. R. Gansch, S. Kalchmair, P. Genevet, T. Zederbauer, H. Detz, A. M. Andrews, W. Schrenk, F. Capasso, M. Loncar, and G. Strasser, "Measurement of bound states in the continuum by a detector embedded in a photonic crystal," *Light Sci. Appl.* **5**, e16147 (2016).
51. K. Y. Bliokh, E. A. Ostrovskaya, M. A. Alonso, O. G. Rodríguez-Herrera, D. Lara, and C. Dainty, "Spin-to-orbital angular momentum conversion in focusing, scattering, and imaging systems," *Opt. Express* **19**, 26132–26149 (2011).
52. L. Allen, S. M. Barnett, and M. J. Padgett, *Optical Angular Momentum* (CRC Press, 2003).
53. L. Marrucci, C. Manzo, and D. Paparo, "Optical spin-to-orbital angular momentum conversion in inhomogeneous anisotropic media," *Phys. Rev. Lett.* **96**, 163905 (2006).
54. D. L. Andrews and M. Babiker, *The Angular Momentum of Light* (Cambridge University, 2012).